

RESEARCH ARTICLE

10.1002/2017JC013402

Impacts of Mesoscale Eddies on the Vertical Nitrate Flux in the Gulf Stream Region

Shuwen Zhang¹ , Enrique N. Curchitser¹, Dajuan Kang¹, Charles A. Stock² , and Raphael Dussin¹¹Department of Environmental Sciences, Rutgers University, New Brunswick, New Jersey, USA, ²NOAA Geophysical Fluid Dynamics Laboratory, Princeton University Forrestal Campus, Princeton, New Jersey, USA

Key Points:

- A high-resolution 25 year simulation in the Gulf Stream region is conducted using a coupled physical-biological model
- Both types of eddies have net positive contributions to the nitrate supply into the euphotic zone
- The eddy-wind interaction-induced Ekman pumping is likely the dominant mechanism for the enhanced nitrate flux at Z_{eu} in ACEs

Supporting Information:

- Supporting Information S1
- Table S1

Correspondence to:

S. Zhang,
shuwen@envsci.rutgers.edu

Citation:

Zhang, S., Curchitser, E. N., Kang, D., Stock, C. A., & Dussin, R. (2018). Impacts of mesoscale eddies on the vertical nitrate flux in the Gulf stream region. *Journal of Geophysical Research: Oceans*, 123, 497–513. <https://doi.org/10.1002/2017JC013402>

Received 30 AUG 2017

Accepted 23 DEC 2017

Accepted article online 8 JAN 2018

Published online 19 JAN 2018

Abstract The Gulf Stream (GS) region has intense mesoscale variability that can affect the supply of nutrients to the euphotic zone (Z_{eu}). In this study, a recently developed high-resolution coupled physical-biological model is used to conduct a 25-year simulation in the Northwest Atlantic. The Reynolds decomposition method is applied to quantify the nitrate budget and shows that the mesoscale variability is important to the vertical nitrate supply over the GS region. The decomposition, however, cannot isolate eddy effects from those arising from other mesoscale phenomena. This limitation is addressed by analyzing a large sample of eddies detected and tracked from the 25-year simulation. The eddy composite structures indicate that positive nitrate anomalies within Z_{eu} exist in both cyclonic eddies (CEs) and anticyclonic eddies (ACEs) over the GS region, and are even more pronounced in the ACEs. Our analysis further indicates that positive nitrate anomalies mostly originate from enhanced vertical advective flux rather than vertical turbulent diffusion. The eddy-wind interaction-induced Ekman pumping is very likely the mechanism driving the enhanced vertical motions and vertical nitrate transport within ACEs. This study suggests that the ACEs in GS region may play an important role in modulating the oceanic biogeochemical properties by fueling local biomass production through the persistent supply of nitrate.

1. Introduction

The Gulf Stream (GS) region, hereafter defined as the area after GS separates from the coast near Cape Hatteras and before it reaches the Grand Banks, is one of the most energetic regions of the world ocean. Mesoscale eddies of the GS, often referred to as GS rings, are frequently generated as a result of baroclinic and barotropic instability processes (Chelton et al., 2011b). Being predominantly nonlinear, these eddies trap fluid in their interiors and transport accompanied physical, chemical, and biological properties as they propagate (Chelton et al., 2007, 2011a, 2011b). In the past few decades, many studies have used in situ and satellite observations and results of numerical models to describe the horizontal structure, dynamic, and kinematic properties of eddies in the GS (e.g., Castelao, 2014; Olson et al., 1985). Recently, a detailed statistical study based on a 50-year high-resolution regional ocean model hindcast was performed by Kang and Curchitser (2013, 2015) and Kang et al. (2016).

Mesoscale eddies affect biogeochemical processes in the ocean, such as the supply of nutrients to the euphotic zone and primary productivity, which are of central importance to the carbon budget of the ocean and marine resources. Early observations of GS eddies reveal that cyclonic eddies (CEs) contain anomalously cold water with elevated concentrations of phytoplankton and nutrients, while anticyclonic eddies (ACEs) incorporate anomalously warm water and low concentrations of phytoplankton and nutrients. This result, based on in situ surveys, is supported by McGillicuddy et al. (1997, 2003), who use a simplified biological model coupled with a quasi-geostrophic ocean circulation model to show that CEs have a positive impact on primary production by inducing a significantly higher input of nutrients to the euphotic zone than surrounding waters. In contrast, ACEs exert an opposite influence by subducting nutrients and creating a relatively unproductive nutrient-depleted surface layer (e.g., McGillicuddy et al., 1999). Alternatively, there also exist observational evidence for enhanced sources of nutrients within an ACE in the North Atlantic Ocean (Woodward & Rees, 2001). Concurrently, Martin and Richards (2001) used a simple model based on an ageostrophic scheme to investigate such ACEs. They demonstrate that ageostrophic upwelling produced by perturbations to the circular flow coupled with wind-induced Ekman pumping can produce a significant flux of deep nutrients to the surface waters. This apparent discrepancy with past work emerges due to the different

perspectives used, with some studies focusing on the net impact of mesoscale variability on biology integrated over a larger region, and others on examining the synoptic view from several snapshots of an individual eddy.

Due to the lack of long-term observations, a high-resolution coupled physical-biological modeling approach can be used to better understand the overall role of eddies in sustaining the rates of nutrient supply to the euphotic zone. Furthermore, a combination of the aforementioned perspectives is required in order to describe the properties of biogeochemical tracers averaged over multiple individual eddies. In this study, we aim to assess the nitrate transports resulted from mesoscale variability by applying Reynolds decomposition method (McGillicuddy et al., 2003; Nagai et al., 2015); then we focus on quantifying the overall effects of CEs and ACEs by using an eddy-centric perspective (Castelao, 2014; Chenillat et al., 2016; Gaube et al., 2013, 2014; Gaube & McGillicuddy, 2017) based on daily samples extracted from a 25-year simulation generated with a three-dimensional physical-biological coupled model of the GS region. Our methods are described in section 2. In section 3, the simulated mean state of the nutrients field over the study area is presented, followed by a description of the time-dependent nutrient flux variations distributed in the horizontal and vertical directions. Then, we apply recently developed eddy detection and eddy tracking algorithms (Kang & Curchitser, 2013) to identify the CEs and ACEs, investigate their roles in locally enhancing or decreasing biological tracer concentrations, and track those changes to the bottom of euphotic zone. A discussion of the mechanisms of eddy-induced vertical supply of nutrient to the euphotic zone is provided in section 4, and a summary of this study is presented in section 5.

2. Methods

We begin by introducing a novel coupled physical-biological model setup to simulate multiyear ocean and ecosystem variability for the entire Northwest Atlantic (NWA). Then, the analysis methods used to obtain and quantify mesoscale variability and its impact on the euphotic zone are described.

2.1. Numerical Model

The physical ocean circulation model used for this study is based on the Regional Ocean Modeling System (ROMS), which solves the hydrostatic, primitive equations with horizontal curvilinear and vertical terrain-following sigma coordinates (Shchepetkin & McWilliams, 2005). The model domain covers the U.S. shelf, slope, and the major path of the Gulf Stream (Figure 1). We employ a grid configuration with a horizontal spacing of 7 km and 40 vertical terrain-following levels stretched toward the surface, with the highest resolution of 0.24 m near surface and the lowest resolution of 250 m at depth. The initial and open boundary conditions are derived from a global reanalysis data set Simple Ocean Data Assimilation version 2.1.6 (SODA v2.1.6) (Carton & Giese, 2008), which provides 5-day averaged data with horizontal 0.5° resolution, 40 vertical layers, and covers the time period of 1958–2008. The atmospheric components, including sea surface temperature, sea level air temperature, pressure, relative humidity, shortwave and longwave radiations, and 10 m winds, are extracted from the Coordinated Ocean-ice Reference Experiments (CORE.v2) data sets

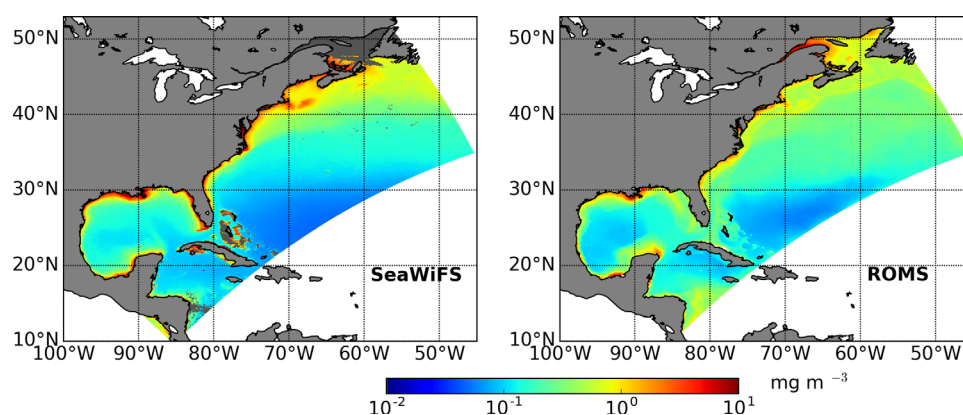


Figure 1. Mean surface chlorophyll concentration for the years 1998–2007 from SeaWiFS observation and the coupled ROMS-COBALT simulation over the entire NWA domain.

(Large & Yeager, 2009) with 6 h intervals. We use the bulk formula of Large (2005) to derive air-sea heat and momentum turbulent fluxes from atmospheric variables, in which the wind is relative to the surface ocean current. Ten major tidal components are extracted from the global ocean tides model TPXO (<http://volkov.oce.orst.edu/tides/global.html>). The barotropic and baroclinic time steps for the model are set to 30 and 240 s, respectively. More details about the model configuration and the evaluation of the physical model performance used in this study can be found in Kang and Curchitser (2013, 2015) and Kang et al. (2016).

The biogeochemical model used here is based on the NOAA/GFDL's Carbon, Ocean, Biogeochemistry and Lower Trophics (COBALT) model (Stock et al., 2014a), which has been developed and used for long time scale climate applications in GFDL's Earth System Models (Stock et al., 2014b). Planktonic food web dynamics in COBALT are represented with a size-structured nutrient-phytoplankton-zooplankton formulation that draws heavily from allometric constraints to represent plankton physiology and consumer prey interactions. There are 33 state variables in the global-scale COBALT, including four types of nutrients, three phytoplankton classes, three zooplankton classes, free-living bacteria, and several detrital pools, with the purpose of resolving the biogeochemical cycles of nitrogen, carbon, phosphate, silicate, iron, calcium carbonate, oxygen, and lithogenic material. COBALT has been ported to ROMS and forms part of ROMS kernel. The North-west Atlantic GS region and shelf of interest for this study are nitrogen limited (e.g., Townsend & Ellis, 2010). We thus simplified the global COBALT implementation by removing phosphorus and iron dynamics, reducing the number of state variables by 11, and also setting the parameter of diazotrophs growth rate to zero.

The initial and boundary conditions for the nitrate, silicate, and dissolved oxygen are derived from World Ocean Atlas 2013 climatologies (Garcia et al., 2014, <https://www.nodc.noaa.gov/OC5/woa13/>), other biogeochemical fields are extracted from the climatological global COBALT results of 1980–2007 (Stock et al., 2014a). Nutrient exports at river mouths are interpolated based on the Global Nutrient Export from Watersheds (NEWS) model (Mayorga et al., 2010), which uses historical data during 1970–2000 to provide river inputs to the ocean of nitrogen, phosphorus, silica, and carbon in dissolved inorganic (N, P, Si), dissolved organic, and particulate (N, P, C) forms.

The coupled model is initialized from SODA v2.1.6 (Carton & Giese, 2008) with the state of 1 January 1980, and then integrated for the subsequent years from 1980 to 2007. To ameliorate effects from the spin-up stage, we discard the first 3 years. Daily averages of the 25-year period during 1983–2007 of hydrographic fields and nitrate concentrations are archived in order to examine how the mesoscale variability impacts the nutrients supply in GS region. The physical properties of this simulation have been described in Kang and Curchitser (2013), who showed that the model produced realistic patterns of large-scale circulation and eddies. COBALT has been shown to recreate large-scale patterns in biogeochemical and plankton dynamics across ocean biomes (Stock et al., 2014b) and across coastal large marine ecosystems (Stock et al., 2017). For the purposes of this study, we limit ourselves to establishing fidelity with the climatological nitrate and surface chlorophyll fields and their water mass associations before conducting a detailed analysis of how eddies operate within these mean fields. The nitrate climatology was taken from the World Ocean Atlas (Garcia et al., 2014) and chlorophyll was drawn from the Sea-Viewing Wide Field-of-View Sensor (SeaWiFS) (NASA Goddard Space Flight Center, Ocean Biology Processing Group, 2014).

2.2. Reynolds Decomposition of the Nitrate Transports

The contribution of mesoscale variability (including transient meanders, mesoscale eddies, and filaments) to the nitrate budget is quantified by using the Reynolds decomposition method (McGillicuddy et al., 2003; Nagai et al., 2015) written as follows:

$$\frac{\partial}{\partial x} (\overline{u'N'}) = \frac{\partial}{\partial x} (\overline{uN}) - \frac{\partial}{\partial x} (\overline{u}\overline{N}) \tag{1}$$

$$\frac{\partial}{\partial y} (\overline{v'N'}) = \frac{\partial}{\partial y} (\overline{vN}) - \frac{\partial}{\partial y} (\overline{v}\overline{N}) \tag{2}$$

$$(\overline{w'N'})_{z_{eu}} = (\overline{wN})_{z_{eu}} - (\overline{w}\overline{N})_{z_{eu}} \tag{3}$$

In the above equations, the overbar symbol indicates the temporal mean of the variables (u , v , and w represent the velocities and N is the nitrate concentration) and the prime symbol represents the temporal perturbations associated with mesoscale variability. The terms on the left-hand side represent the contributions

from the mesoscale variability. The fluxes associated with the perturbations will be referred to as the eddy-induced fluxes in section 3.3. Z_{eu} represents the depth of the euphotic zone, which is defined as the depth where photosynthetic available radiation (PAR) is 1% of its surface value.

Considering the mesoscale eddies in the ocean persist with time scales from days to months but rarely longer than a year, we obtain the temporal mean variables by annually averaging the daily mean outputs during the 25-year simulation period. With this choice of temporal average, the interannual variations and the transient variations with time scale less than a day are excluded from the perturbations in (1)–(3). It is worth noting that the eddy-induced fluxes obtained by Reynolds decomposition method contain contributions not only from mesoscale eddies but also from other mesoscale features (e.g., GS meanders, mesoscale filaments). In order to precisely investigate the effects of individual eddies, an appropriate eddy detection and tracking algorithm is required.

2.3. Eddy Detection and Tracking

We apply the Kang and Curchitser (2013) eddy detection and eddy tracking algorithms to the sea surface physical properties, including the velocity and sea surface height fields, over the 25-year simulation period. The algorithm incorporates a series of geometrical constraints to enhance the eddy detection accuracy and the capability of capturing the irregular shapes of eddies during their evolution. Moreover, the eddy detection and eddy tracking algorithms can effectively detect mesoscale eddies with enclosed surface circulation and exclude Gulf Stream meanders. Detailed procedures can be found in Kang and Curchitser (2013), where the evaluation of simulated eddy characteristics in the GS region, including the eddy size, duration, intensity, propagation, spatial distribution, evolution, and seasonal variability, are also presented. In this study, we use the same physical model configuration, and therefore the validation of the physical eddy characteristics is not shown.

In order to describe the hydrography and biological properties in the detected eddies, we first interpolate the model output from terrain-following to geopotential coordinates between the surface and 500 m with an interval of 5 m. Then, at the depth of 500 m we apply the same eddy detection method. When a detected eddy at 500 m meets the constraints that (a) its center remains in the area of the one detected at surface and (b) its equivalent radius is greater than 25 km, we treat this as a single, depth-coherent eddy. Our choice of 500 m is less than the observed depths of some eddies (Castelao, 2014; $\sim 1,000$ m), but reflects our interest in processes either within or immediately below the euphotic zone. The center position, radius, and polarity (cyclonic and anticyclonic) of eddies satisfying these criteria are then saved.

Eddies are tracked in the daily averaged output by comparing eddy center positions and radii at consecutive days within the neighboring area of 10×10 grid points over the entire simulation period. Only eddy durations longer than 15 days are tracked. Occasionally, there are daily-gaps in eddy trajectories when the eddies fail to pass the identification criteria due to strong deformation events. We retain these eddies by smoothing the temporal gaps between consecutive days due to the fact that the physical variations which induce nutrient supply at the oceanic mesoscale are on the order of weeks (McGillicuddy et al., 1999).

2.4. Eddy Composite Analysis

In order to investigate the vertical and radial structure in the mesoscale eddies, we performed an average eddy analysis—or eddy composite analysis—on all the detected eddies (Chelton et al., 2011a). Along the trajectory of an eddy, for each daily output, we take the eddy centroid as the coordinate origin; then the model results within a circular area with a radius of R are extracted, where R is the equivalent radius of the individual eddy (defined as the radius of the circle with the same area enclosed by this eddy boundary). The selected area includes both the eddy and its surrounding water. The horizontal coordinates ($-2R$ to $2R$) for each eddy are normalized by the R and then each daily eddy snapshot is objectively remapped onto a new uniform normalized coordinates (-2 to 2) with an interval of 0.1. By this means, the composites of the physical and biogeochemical variables can be obtained by averaging the daily eddy snapshots on this normalized coordinate system (the edge of the eddy is at the normalized radius of 1). Since our purpose is to quantify the net contribution of large sample of eddies, the composite analysis is based on averaging all detected CEs and ACEs, regardless of their life stages.

3. Results

The coupled ROMS-COBALT simulation results are archived daily for the 25-year period from 1983 to 2007. We first evaluate the model performance with respect to the climatological mean surface chlorophyll concentrations and net primary production (NPP) (section 3.1). Then, we evaluate the simulated nitrate field in GS region and present the mean nitrate distributions (section 3.2). The overall impact of mesoscale eddies on the nitrate budget is assessed by conducting a temporal Reynolds decomposition analysis (section 3.3). Next, individual eddies are detected and tracked during the 25-year simulation period, and the composite analysis on all the identified eddies is performed (section 3.4). This is used to quantify the vertical and radial structure of properties in both CEs and ACEs. Finally, the long-term contributions of CEs and ACEs to the vertical nitrate flux are quantified (section 3.5).

3.1. Surface Chlorophyll and Net Primary Production Comparisons

Chlorophyll concentrations from the Sea-Viewing Wide Field-of-View Sensor (SeaWiFS) during 1998–2007 are compared with the ROMS-COBALT simulated chlorophyll during the same period (Figure 1). The model captures large-scale spatial chlorophyll variability in the NWA domain seen in the SeaWiFS climatology, including the cross-shelf gradient with averaged values as high as 3 mg m^{-3} on the shelf to less than 0.1 mg m^{-3} in the Sargasso Sea. The model underestimates chlorophyll in Georges Bank and Nantucket Shoals are subject to strong tidal mixing. A comparison focusing on the GS region is made between the simulated and the satellite-derived NPP (Figure 2), which is estimated via the “Eppley” version of the Vertically Generalized Production Model (Eppley-VGPM) from the Ocean Productivity (<http://www.science.oregon-state.edu/ocean.productivity>). The NPP in COBALT is diagnosed during the model integration, in which the 100 m depth is assigned as a proxy of the euphotic depth for the purpose of calculation efficiency. Both the model and the observation present NPP values higher than $300 \text{ g C m}^{-2} \text{ yr}^{-1}$ in the slope sea adjacent to the Mid-Atlantic Bight. Productive waters of $\sim 180 \text{ g C m}^{-2} \text{ yr}^{-1}$ are located north of 36°N ; in contrast to these high primary productivity levels, the mean NPP in the Sargasso Sea is less than $100 \text{ g C m}^{-2} \text{ yr}^{-1}$.

3.2. Climatological Mean of the Nitrate Field

For the present study, we select the region covering the northeast U.S. shelf, continental slope and GS area, and focus on the mean state of the nitrate field. Figures 3a and 3b present the comparison of the nitrate field averaged in the upper 100 m depth between the 25 year simulated climatology and the climatological estimates from the World Ocean Atlas 2013 (WOA13, Garcia et al., 2014). The model captures the general gradient of upper 100 m nitrate concentration, exhibiting high values over the shelf and decreasing in the offshore oligotrophic waters with deep nutriclines. The isopleths of nitrate approximately parallel isobaths. There are contiguous patches of nitrate concentrations higher than 8 mmol N m^{-3} extending from the Nova Scotia shelf to Cape Hatteras as shown in Figure 3b. The nitrate increase over the shelf is the combined result of seasonal convective mixing with nutrient-rich waters near the bottom as well as the frequent intrusions of Warm Slope Water, which is characterized by its high nutrient concentrations below the surface (Townsend & Ellis, 2010). At the offshore area near 36°N associated with the GS separation point, the

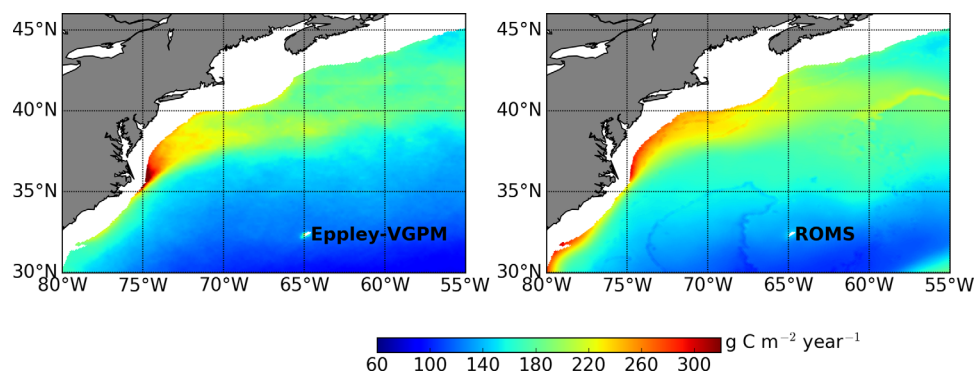


Figure 2. Mean net primary production (NPP) from the Eppley-VGPM estimates of SeaWiFS observation and the upper 100 m integrated diagnostic from coupled ROMS-COBALT simulation. The shelf area with water shallower than 300 m is not plotted to highlight the NPP values in GS region, which is the area of interest in this study.

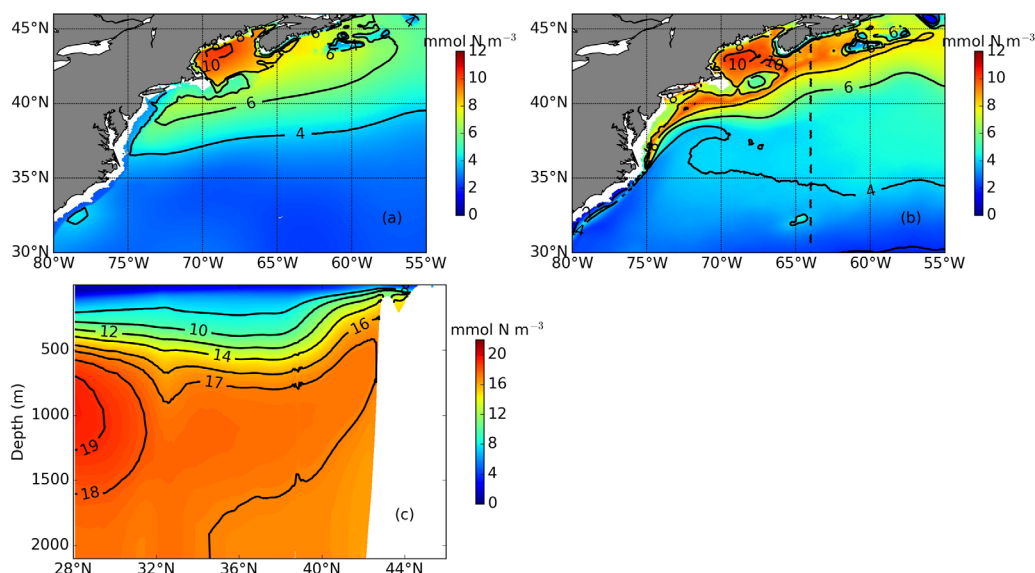


Figure 3. The upper 100 m depth averaged concentrations from (a) World Ocean Atlas 2013 and (b) simulation results averaged during 1983–2007. The coastal area with water shallower than 30 m is neglected to avoid the complexity of nutrients supplied by river runoff, and for water depth shallower than 100 m over the shelf, the vertical average of nitrate in the whole water column is used. The black dashed line in Figure 3b represents the vertical section along 64°W shown in Figure 3c. (c) Nitrate distribution in the meridional section at 64°W extending from 100 m depth off Nova Scotia shelf to the south boundary of the model domain.

model captures the nitrate rich waters extending to the slope off the Mid-Atlantic Bight. The 6 mmol N m^{-3} isopleth of nitrate then turns northeastward toward the Grand Bank.

The above-described plan view of the upper 100 m averaged nitrate field indicates nitrate concentrations are associated with different water masses. To demonstrate this, we select a meridional section at 64°W (dashed line in Figure 3b), extending from 100 m depth off Nova Scotia shelf to the south boundary of the model domain. It partially overlaps with a section across the GS in the World Ocean Circulation Experiment (WOCE) Hydrographic Program. In Figure 3c, from 38°N southward, the nitrate is depleted in the upper 100 m, resulting in the oligotrophic North Atlantic subtropical gyre; the nitrate concentration is enriched at depth, forming a layer featured by a sharp increase gradient between 300 and 500 m and up-tilting northward across the slope to the shelfbreak. Subsurface slope waters are highlighted by the 17 mmol N m^{-3} contour and known as a combination of Atlantic Temperate Slope Water (ATSW, higher than 17 mmol N m^{-3} between 500 and 1,500 m) and Labrador Subarctic Slope Water (LSSW, lower than 17 mmol N m^{-3}). All the above features of nitrate distributions are consistent with the WOCE observation across this section from Knapp (1988, their Figure 9).

3.3. Nitrate Budget Analysis

In this section, we present the analysis of the nitrate budget in a region that is characterized with energetic mesoscale eddy activity (Kang & Curchitser, 2013). The top plot of Figure 4 shows the 25-year averaged horizontal advection, vertical advection, and vertical mixing terms vertically integrated within the euphotic zone (Z_{eu}). Note the vertically integrated vertical advection and vertical mixing terms are simply the fluxes at the base of the euphotic zone. The turbulent mixing term (Figure 4c) is always positive and shows a relatively weak increasing tendency from open ocean to shelfbreak, while the other two terms have considerably large spatial variations. The averaged supply of nitrate in the euphotic zone by the combination of the three terms is $0.517 (\pm 0.638) \text{ mol N m}^{-2} \text{ yr}^{-1}$ in the selected region. If we convert this nitrate supply to the NPP by using the Redfield ratio (C:N = 6.625) and an empirical f-ratio (0.26 for Atlantic ocean (Eppley & Peterson, 1979)), the value of the estimated NPP ($158 \text{ g C m}^{-2} \text{ yr}^{-1}$) is comparable with the domain-averaged observed and modeled NPP (155 and $164 \text{ g C m}^{-2} \text{ yr}^{-1}$) shown in Figure 2.

The Reynolds decomposition of the horizontal and vertical advection terms (Figures 4d–4g) illustrate the relative importance of the mean and eddy-induced horizontal and vertical transports. Note the eddy-

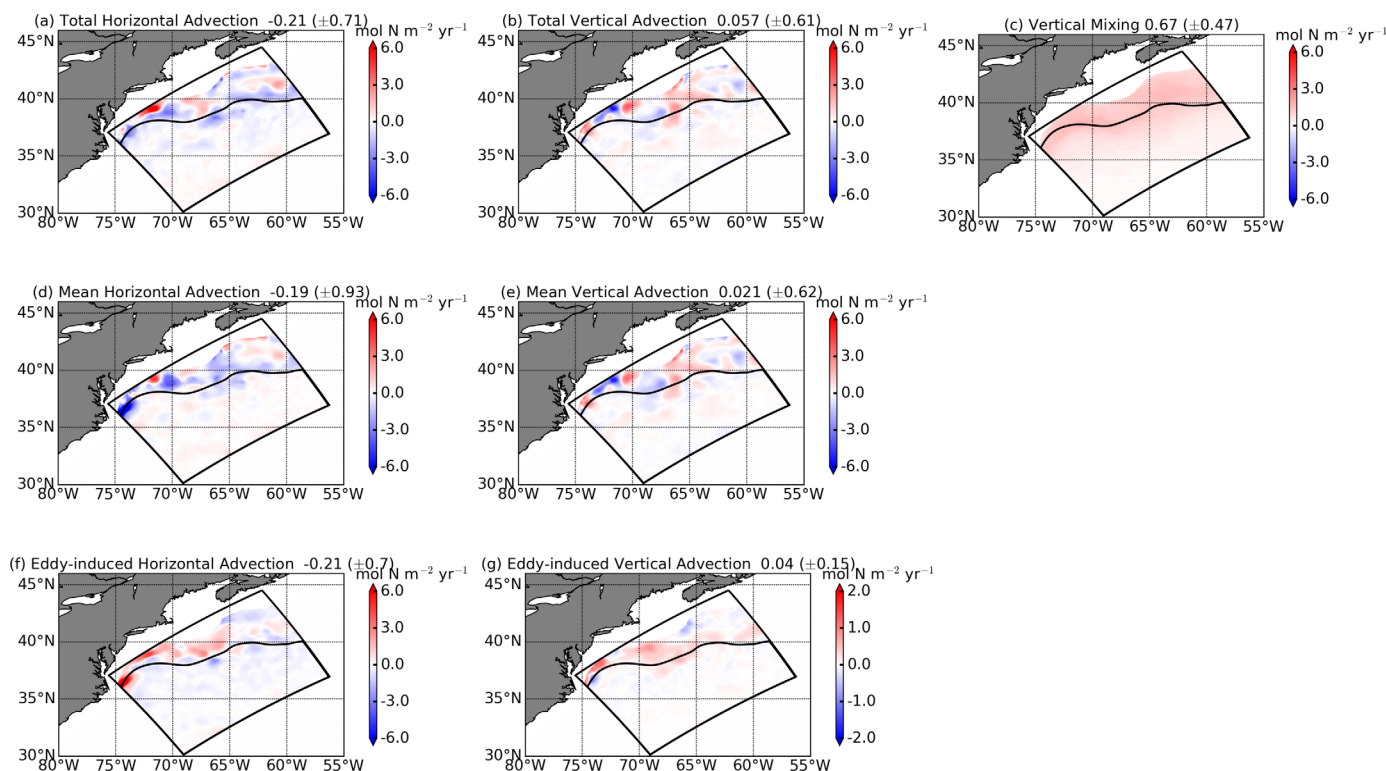


Figure 4. The 25 year averaged nitrate budget terms integrated over the euphotic zone from the model simulation: (a) total horizontal advection, (b) total vertical advection, (c) total vertical mixing. (d) and (e) The mean horizontal and vertical advection terms obtained by the Reynolds decomposition, respectively. (f) and (g) The eddy-induced horizontal and vertical advective fluxes obtained by the Reynolds decomposition, respectively. All the fields are smoothed by a 3×3 median filter. The black contour represents the simulated position of the 15°C isotherm at 200 m depth, which represents the mean GS pathway. The shelf regions with water depth shallower than 300 m are excluded. The black rectangles outline the study domain used for eddy detection and analysis. The area-averaged value of each nitrate budget term within the black rectangle is listed in the title of each plot with standard deviation in the parentheses. Note the color range of Figure 5g is a quarter of that in the other plots.

induced transports include contributions from all mesoscale features, including mesoscale eddies, GS meanders, mesoscale filaments, etc. The eddy-induced advection terms (Figures 4f and 4g) have comparable magnitude to the mean advection terms (Figures 4d and 4e). The pattern of the mean vertical flux (Figure 4e) resembles that of the total flux (Figure 4b). The most significant mean vertical flux occurs in the area adjacent to the path of the Gulf Stream. Considering that the mean vertical flow only contains variations with time scale above a year (section 2.2), the spatial distribution of the mean vertical flux (Figure 4d) is likely determined by a combination of the interannual variability of the Gulf Stream and the interaction of the mean current with topography. In contrast to the mean vertical flux that possesses alternating positive and vertical values, the 25-year averaged eddy-induced vertical flux is mostly positive over the selected region (Figure 4g). The area-averaged eddy-induced vertical flux ($0.040 \text{ mol N m}^{-2} \text{ yr}^{-1}$) is almost two times of the area-averaged mean vertical flux ($0.021 \text{ mol N m}^{-2} \text{ yr}^{-1}$). This indicates the mesoscale features play an important role in the nitrate supply in the euphotic zone over the area of interest. However, as described in section 2.2, the Reynolds decomposition method cannot isolate the contribution of coherent mesoscale eddies to the vertical nitrate supply from other mesoscale features. In the following section, we turn to examine the impact of individual mesoscale eddies.

3.4. Composite Structures of CEs and ACEs

The individual mesoscale eddies within the area selected previously are detected by applying the eddy detection and tracking algorithms developed by Kang and Curchitser (2013). A summary of eddy properties is listed in Table 1, and is similar to those from the 50-year simulation in Kang and Curchitser (2013). It should be noted in Table 1 the eddy duration refers to the period during which the extracted eddies continuously meet the detection criteria, which is not an equivalent concept to the life span of these eddies. We applied several strict criteria (described in details by Kang and Curchitser (2013)) to identify the coherent

Table 1
Eddy Properties in the Study Domain With Standard Deviations in the Parentheses

	Number		Duration (days)	Radius (km)	Distance (km)	Westward propagation speed (km d ⁻¹)
	Total in 25 years	Average per year				
CE	612	24 (±5.3)	46 (±20.63)	88 (±21.2)	193 (±72.1)	3.8
ACE	740	30 (±5.5)	31 (±7.5)	81 (±27.7)	167 (±39.6)	2.5

eddies and separate them from other mesoscale features, such as GS meander and mesoscale filament. We notice any given eddy can only satisfy the detection and tracking criteria during a certain portion of its entire life span, i.e., an eddy which has a long decay period may not be fully tracked. Thus, it is expected that the duration of the eddies listed in Table 1 (31 days for ACE and 46 days for CE) are shorter than previous reported based on in situ (e.g., 361 days for longest CE and 152 days for longest ACE from Richardson (1993)) or satellite observations (e.g., most eddies are longer than 15 weeks shown in Figure 5c of Gaube and McGillicuddy (2017)). The seasonality of the eddy statistics in this study is largely consistent with Kang and Curchitser (2013) and will not be discussed here. The monthly distributions of number and mean intensity of the eddies in this study are provided in supporting information.

Figure 5 shows all of the detected eddy centers at each grid point in the interior of the study domain to illustrate the spatial occurrence and dominance of CE and ACE in the 25-year simulation. The black contour indicates the mean GS pathway. Following the definition of Joyce et al. (2000), GS is defined by the position of the 15°C isotherm at 200 m depth. Consistent with previous observational studies (Richardson, 1983), there are general tendencies for CEs and ACEs to pinch off from the southern (Figure 5a) and the northern (Figure 5b) sides of the GS, respectively. In our study region, CEs mostly occur on the southern side of the mean GS path between 35°N and 38°N, while ACEs mostly occur on the continental slope from southeast of Georges Bank up to Scotia Slope near 1,000 m isobaths.

We next proceed to examine the composite hydrography and nitrate fields within CEs and ACEs and their surrounding waters created based on the method described in section 2.4. The radius-depth distributions of the hydrographic fields of CEs and ACEs demonstrate distinct features and are shown in Figure 6. For the temperature field (Figures 6a and 6d), the isotherms in CEs form a dome with the 22°C isotherm raised upward toward the surface and the 20°C isotherm is uplifted approximately 50 m from the edge to the core of the eddy. In comparison, ACEs have a relatively weak (less than 10 m) depression in the eddy core in the upper 50 m. The downward signature is more apparent at depth below 50 m: the 20°C isotherm at the eddy edge is around 100 m, while it is pushed down to 200 m at the eddy center. For the salinity field (Figures 6b and 6e), the low salinity waters in CEs are displaced upward to 100 m and maintain a relatively uniform profile in the upper water column. In ACEs, vertical displacements of salinity show a subsurface salty-core feature at about 100 m depth, which is 0.05 psu higher than the ambient water. This is consistent with the previous observations showing that the Gulf Stream system has a subsurface salinity maximum, which is usually observed at 90–130 m depth below the surface (Castelao, 2014; World Ocean Atlas, 2013 by

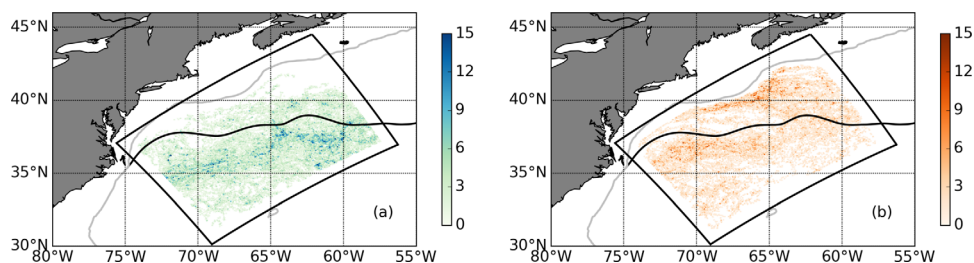


Figure 5. The spatial distributions of eddy center occurrences for all (a) CEs and (b) ACEs identified in the GS region during the 25 year simulation period. Color represents the eddy center occurrences at given locations. The black contours represent the climatological GS pathway in both plots. The 1,000 m isobath is shown as the gray line to denote the shelfbreak. No eddies are detected on the inner eight grid points along the boundaries of the study domain.

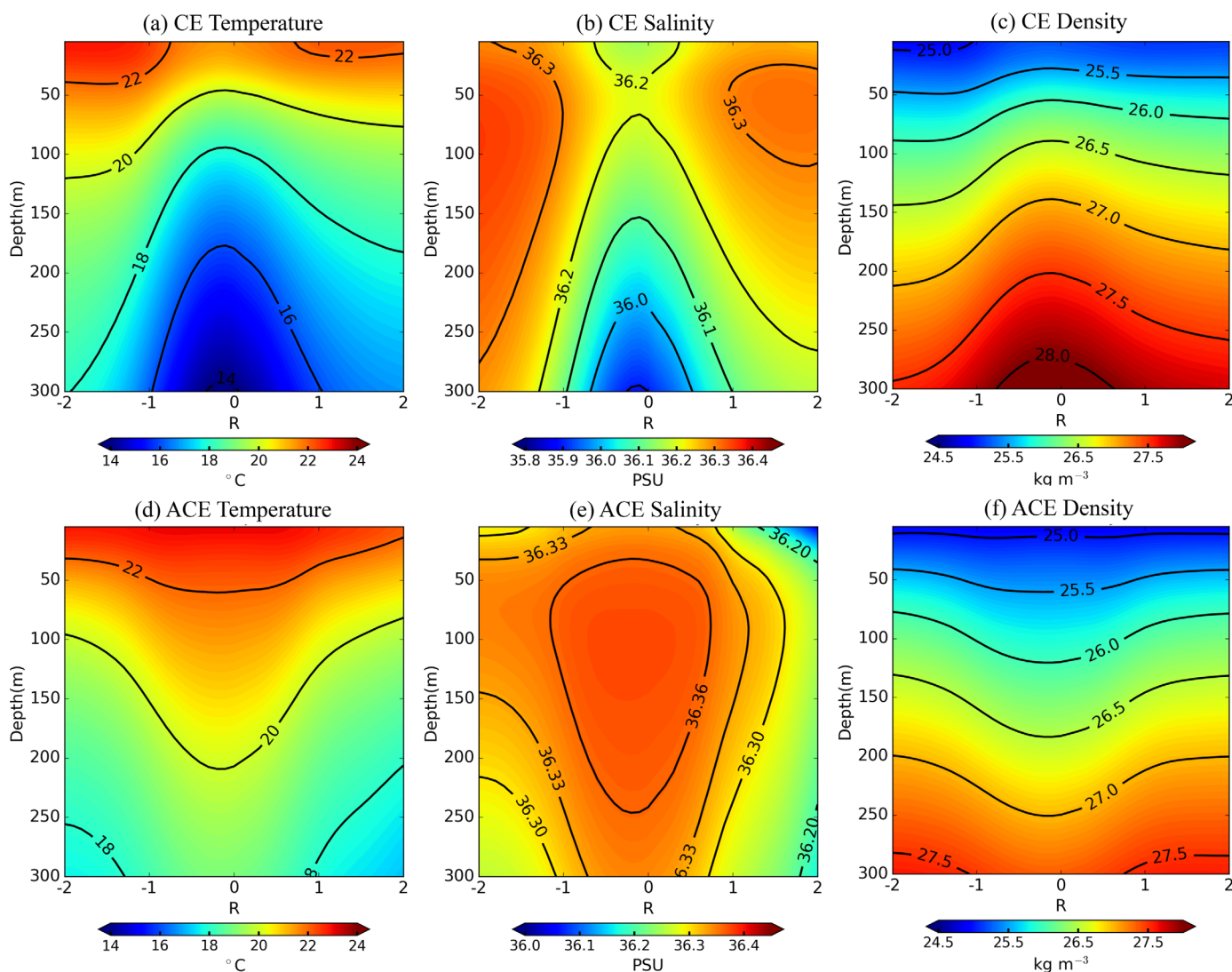


Figure 6. The composite temperature, salinity, and potential density in (a, b, c) cyclonic eddies (CEs) and (d, e, f) anticyclonic eddies (ACEs) tracked during the 25 year simulation period. The transects are latitudinal across the eddy center and x axis is the normalized radius (defined in the text); negative (positive) radii are to the south (north) of the eddy center. The contour intervals are 2°C for temperature and 0.5 kg m^{-3} for density. Note different color scales for salinity are used for CE and ACE to better demonstrate the spatial variations.

Garcia et al., 2014). The subsurface salinity maximum is believed to originate from the northward advection of the North Atlantic subtropical underwater and saline Central Water (Talley et al., 2011, Chapter 9, Atlantic Ocean). A slightly asymmetric feature, with higher temperature and salinity to the left of the eddy centers, exists both in CEs and ACEs. This is because the transects used for the composite analysis are latitudinal sections across the eddy center. The northern sides of the eddies are cooler and fresher than the southern edges. The vertical profiles of temperature and salinity together determine the composite vertical structure of isopycnals, which are domed upward in CE and displaced downward in ACE (Figures 6c and 6f).

The composite nitrate fields for CEs and ACEs are shown in Figure 7. In the upper water column, at depths shallower than 100 m, nitrate concentrations are depleted in both types of eddies, with values ranging from 0 mmol N m^{-3} at surface to 3.0 mmol N m^{-3} at depth. Below 100 m, the nitrate distributions show the similar pattern as that of the temperature field: in CEs, the isopleths shoal toward eddy center and reveal the enhanced nitrate concentration due to the upwelling effects in CEs, while in ACEs, the nitrate contours with values higher than 7.0 mmol N m^{-3} follow a significant concave shape resulting from the downwelling in ACEs (Figures 7a and 7d).

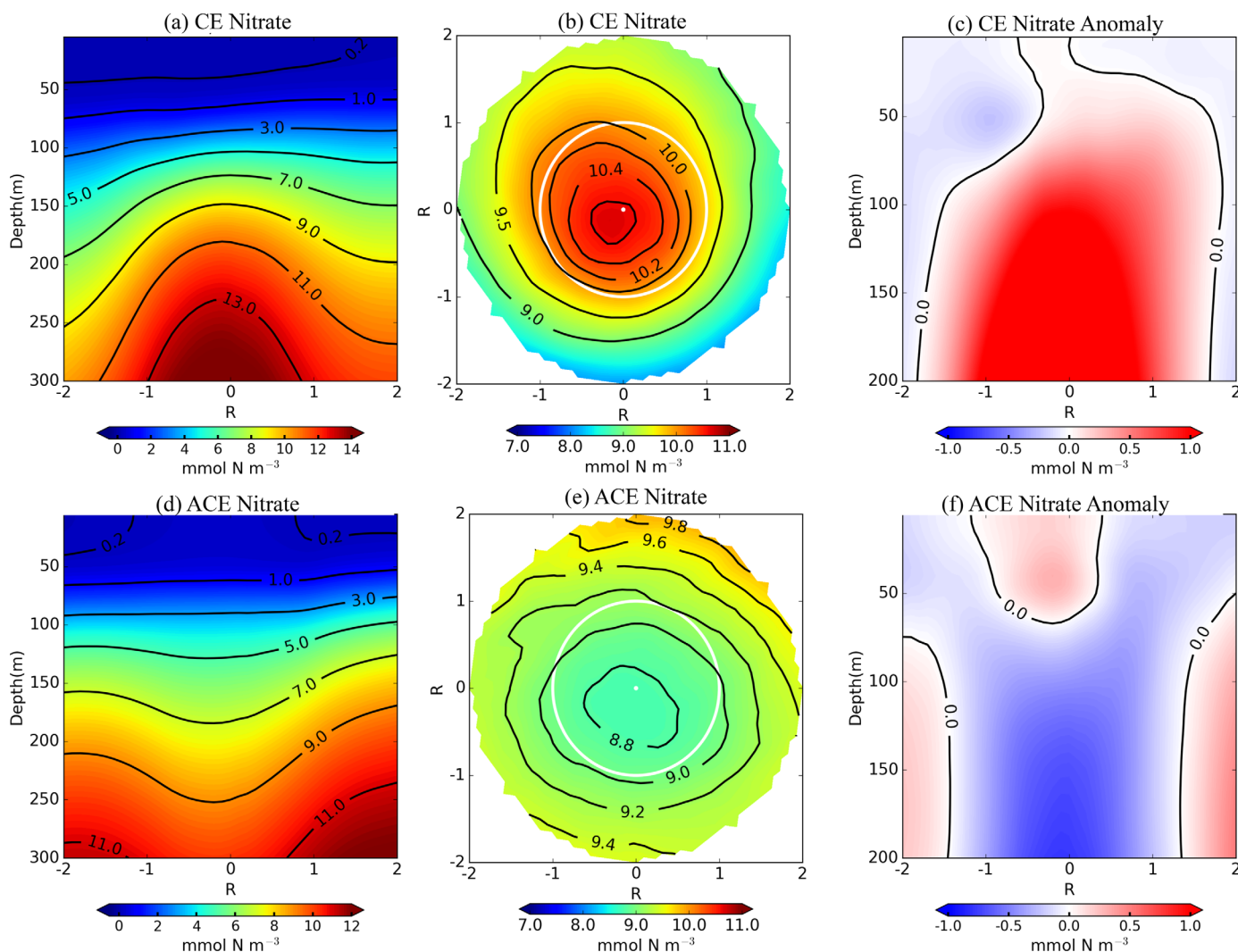


Figure 7. (a, d) Same as Figure 6, but for nitrate. (b, e) Horizontal view of the composite of nitrate at 200 m depth; white circles indicate the eddy equivalent radius, which is R from the eddy center (white dot). (c, f) Same as (a, d) but for nitrate anomaly (defined in the text).

To further examine the above features of CEs and ACEs, a horizontal view of the composite average of nitrate field is constructed at 200 m depth (Figures 7b and 7e). The nitrate contours of 10.0 and 9.0 mmol N m⁻³ approximately overlap the CEs and ACEs peripheries, which are represented as white contours. In the centroids, the nitrate concentrations are found higher than 10.6 and lower than 8.8 mmol N m⁻³, respectively. Such statistical result suggests that in the lower water column, the nitrate concentrations are enhanced in the interior of CEs with an amplitude of 0.6 mmol N m⁻³, while decreased in the interior of ACEs with a smaller amplitude of 0.2 mmol N m⁻³.

We note that nitrate in the ACEs exhibits a doming of nitrate concentration near the ocean surface that contrasts with the concavity of nitrate isopleths at depth (Figure 7d, following the 0.2 mmol N m⁻³ isopleth). This doming disappears approximately at 70 m (following the 1.0 mmol N m⁻³ isopleth), which is beneath the average depth of the euphotic zone (defined as the depth where photosynthetic available radiation (PAR) is 1% of its surface value). During the 25-year simulation period, the euphotic zone is 62 m on average, but varies from 10 to 140 m seasonally. To further illustrate this phenomenon, we construct the composites of eddy-induced nitrate anomalies. For each CEs and ACEs, we first compute the daily nitrate anomaly induced by every individual eddy after subtracting the local annual average from the local daily value of the nitrate field. Then we apply the composite analysis to the computed nitrate anomalies. The radius-depth distributions of the composite nitrate anomalies in the upper 200 m are presented in Figures 7c and 7f.

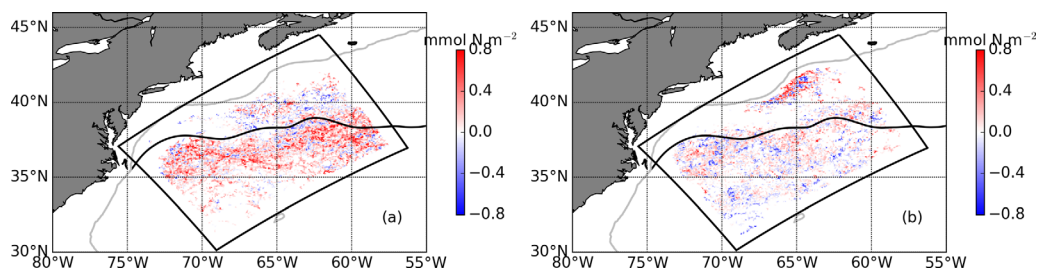


Figure 8. The spatial distributions of nitrate anomalies integrated in the euphotic zone caused by the (a) CE and (b) ACE identified during 1983–2007. The climatological GS pathway is represented as the black contour. The 300 m isobath is shown as the gray line to denote the location of shelfbreak.

Overall, CEs induce positive nitrate anomalies, which gradually decrease upward to the surface. In contrast, the nitrate anomalies associated with ACEs have a more complicated vertical distribution: while the negative anomalies below 70 m are as expected due to the downward displacement of isopycnals in ACEs, positive anomalies are dominant above 70 m. Focusing on the mean euphotic zone depth, which corresponds to 62 m, the positive nitrate anomalies are even more significant inside the ACEs than CEs.

3.5. Total Contribution of Eddies to the Nutrient Supply into Euphotic Zone

The composite positive nitrate anomalies above the euphotic zone in ACEs suggest they are prevalent phenomena. In order to corroborate this finding, we proceed to investigate the spatial distributions of the nitrate anomalies associated with all the detected eddies and quantify the overall contribution of mesoscale eddies to the vertical nutrient supply into euphotic zone.

To obtain the nitrate anomaly associated with each eddy, we subtract the annual mean from the daily nitrate concentration at each point along the trajectory of each eddy. Then we integrate each nitrate anomaly from the surface to the euphotic zone depth to produce a daily map representing the spatial distribution of vertical integrated nitrate anomalies induced by eddies within the euphotic zone. After overlaying all eddies during the 25-year simulation period, the spatial distribution of nitrate anomalies within the CEs and ACEs are presented in Figure 8. In CEs, the nitrate anomalies are dominant by positive values in space; while in ACEs, both the positive and negative nitrate anomalies prevail spatially and nearly distribute equally. This suggests that various mechanisms may act synchronously to transport nitrate vertically within ACEs.

Besides the spatial distribution of nitrate anomalies discussed above, we further quantify the fraction of eddy numbers with positive nitrate anomalies accounting for the total eddy numbers during each year. For each individual eddy, we obtain its net contribution by taking the temporal average of nitrate anomaly within its whole duration. We then calculate the fraction as the ratio between the numbers of eddies with net positive nitrate anomaly and the total numbers of eddies detected in the corresponding year. Results for ACEs and CEs are shown in Figure 9. When ACEs (CEs) causing positive nitrate anomalies within the euphotic zone are dominant in the total ACEs (CEs) numbers, the fraction is larger than 0.5. In Figure 9, the time series show that in most years, the fraction values of both ACEs and CEs exceed 0.5, although there are a few exceptions for ACEs (years of 1991, 1995, 1996, 1999, and 2006). There is apparent interannual

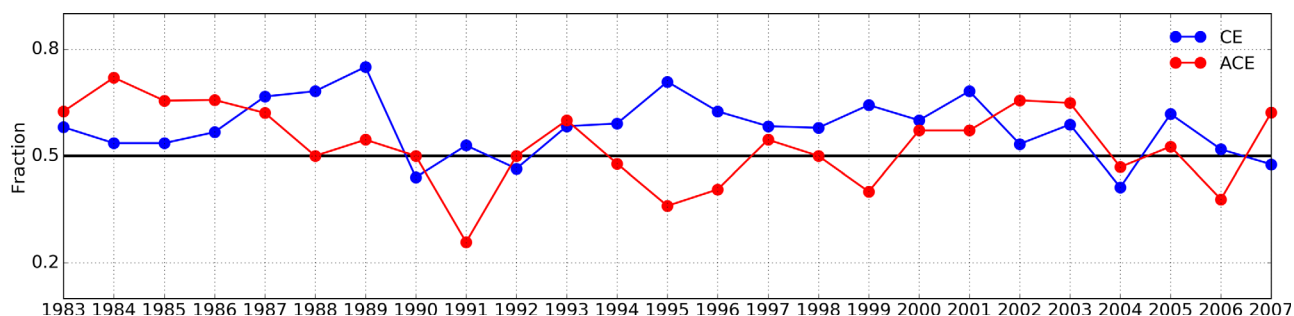


Figure 9. Time series of the fraction of eddies with positive nitrate anomalies integrated within the euphotic zone in total numbers of eddy tracked each year during the 25-year simulation period. The red and blue lines represent the anticyclonic eddies (ACE) and cyclonic eddies (CE), respectively.

variability in the time series of the fraction of eddies with positive nitrate anomalies. We speculate that there are at least two sources of such variability: (1) the interannual variability of the GS pathway, which in turn is under the influence of the atmospheric variability such as the NAO (Taylor & Stephens, 1998) and (2) the interannual variability of the water masses that are characterized with different nitrate concentrations in the northwest Atlantic (Townsend & Ellis, 2010). A detailed examination of these factors is out of the scope of the current study but warrants future study.

Finally, we quantify the mean vertical nitrate supply into the euphotic zone within the two types of eddies. To estimate the vertical nitrate flux supply induced by each detected eddy, we obtain the vertical nitrate flux across the euphotic depth within the periphery of the corresponding eddy and then take the average. On average, the vertical nitrate flux into euphotic zone is $0.07 \text{ mol N m}^{-2} \text{ yr}^{-1}$ inside the CEs and $0.29 \text{ mol N m}^{-2} \text{ yr}^{-1}$ inside the ACEs. Note these values are higher than the domain-averaged vertical flux ($0.057 \text{ mol N m}^{-2} \text{ yr}^{-1}$ shown in Figure 4b), which indicate both CE and ACE enhance the nitrate supply into the euphotic zone. It is worth noting that the averaged vertical nitrate flux within ACEs is four times higher than that within CEs.

4. Discussion on the Mechanism for the Enhanced Nitrate Supply in ACEs

It has long been recognized that mesoscale eddies have vital impacts on the distributions of marine biogeochemical properties over the global ocean. Our analyses, which integrate eddies over 25 simulation years, suggest that in the GS region both ACEs and CEs make a net positive contribution to the nitrate flux into the euphotic zone. In particular, for ACEs we show that the mean tendency for local enhancement of nitrate above the euphotic zone depth is an important feature in the GS region. The mechanisms for the vertical supply of nutrients associated with eddies can be different due to diverse factors including the varying regimes, the path of the eddy's center, the stages of the eddy's life cycle, etc. (e.g., Falkowski et al., 1991; McGillicuddy et al., 1998, 2007; Nagai et al., 2015; Siegel et al., 2011). In the interior of eddies, the conventional view relates vertical velocities to the change of density anomalies during eddy intensification, known as "eddy-pumping" (McGillicuddy et al., 1998). Following this concept, CEs upwell nutrient-rich subsurface water into the euphotic zone and are relatively productive, while ACEs play the opposite role, deepening the nutricline and depleting nitrate in the euphotic zone (McGillicuddy & Robinson, 1997). The positive contribution of CEs on the vertical nitrate transport revealed in this study is consistent with the conventional view. However, the prevalent positive impact of ACEs on the nitrogen budget over the 25 year simulation period is not.

In the following, we investigate the dominant mechanism for the positive nitrate anomalies in the euphotic zone in ACEs. Two possible mechanisms have been described in previous studies. In the first, the relative motion between surface current and wind generates upwelling at the ACE center and downwelling at the CE center. This process is often referred to as "eddy-wind interaction-induced Ekman pumping" (Gaube et al., 2015), which has been suggested as a mechanism to explain enhanced nutrient supply to the surface within ACEs in the North Atlantic (Martin & Richards, 2001; McGillicuddy et al., 2007). In the second mechanism, the mixed-layer depth is modulated by the local changes in stratification driven by eddy-induced vertical isopycnal displacements. The warm SST anomalies in ACEs tend to release heat from the ocean into the atmosphere and thereby enhances the convection in the upper ocean. The tendency for ACEs to have deeper mixed layers than CEs has been noted in the Gulf Stream (Dewar & Flierl, 1987) and the South Indian Ocean (Dufois et al., 2014; Gaube et al., 2013). However, it must be noted differentiating between enhanced vertical mixing and eddy-induced Ekman pumping is difficult based on the observations, as both mechanisms tend to produce similar effects (McGillicuddy, 2016).

Based on the results from our high-resolution model simulation, we are able to examine the nitrate budget and quantify the relative importance of the above two processes, i.e., the enhanced vertical advection and mixing within ACEs. The nitrate budget equation integrated vertically from the base of the euphotic zone to the surface can be written as

$$\frac{\partial |N|}{\partial t} = \underbrace{[wN]_{Z_{eu}}}_{WADV} + \underbrace{\left[-k_z \frac{\partial N}{\partial z} \right]_{Z_{eu}}}_{TMIX} - \left| \frac{\partial uN}{\partial x} \right| - \left| \frac{\partial uN}{\partial y} \right| + |Bio|$$

where $| |$ represents vertical integration from the base of euphotic zone (Z_{eu}) to surface. The above equation indicates that the evolution of the vertical integrated nitrate concentrations is determined by the vertical advection term (labeled as WADV), the vertical turbulent diffusion (labeled as TMIX), and the horizontal

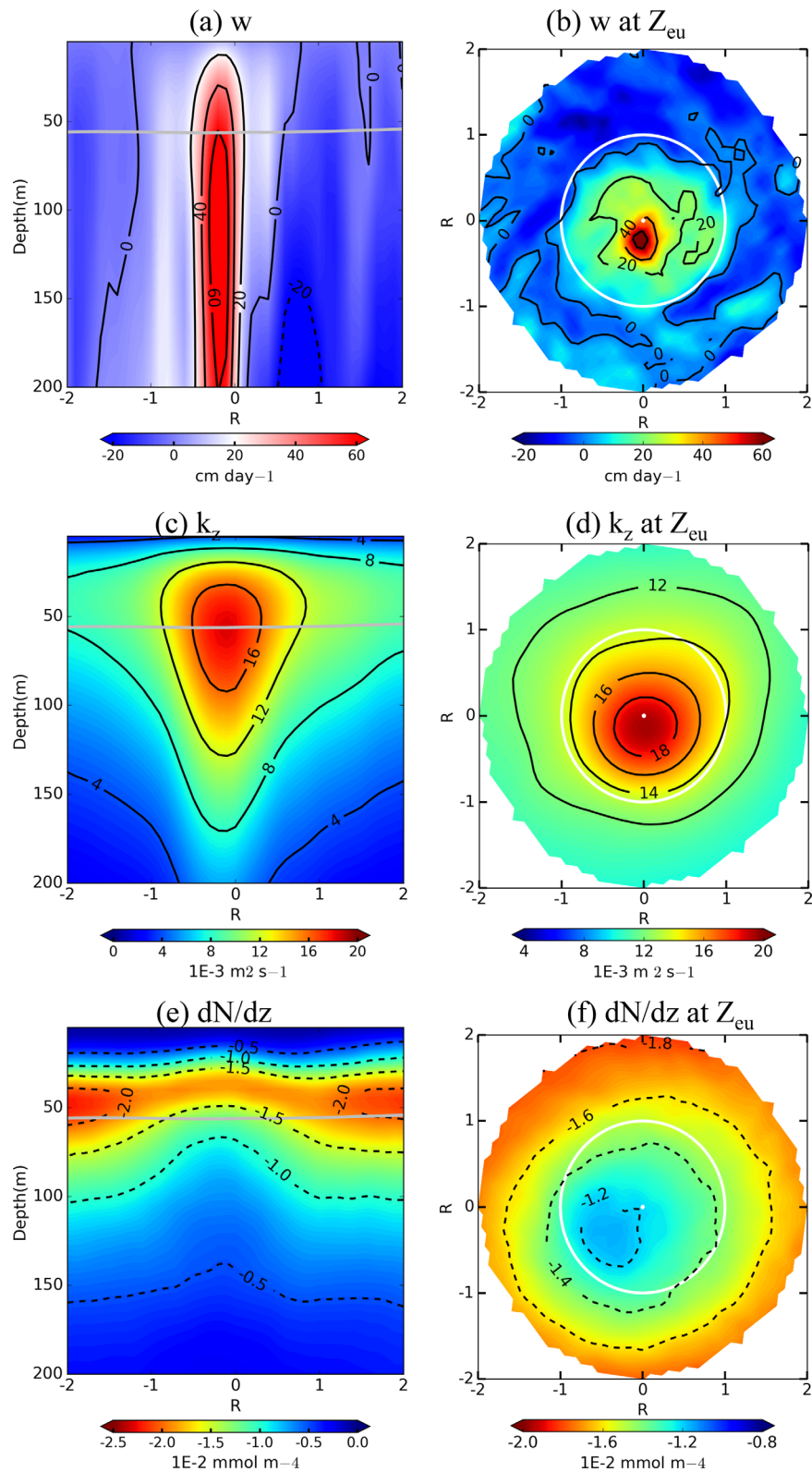


Figure 10. (top) The composite vertical velocity (a) along the latitudinal transects across the ACE center and (b) at the euphotic depth 62 m (the gray thick lines). (middle) Same as (a) and (b) but for the vertical mixing coefficient. (lower) Same as (a) and (b) but for the vertical nitrate gradient.

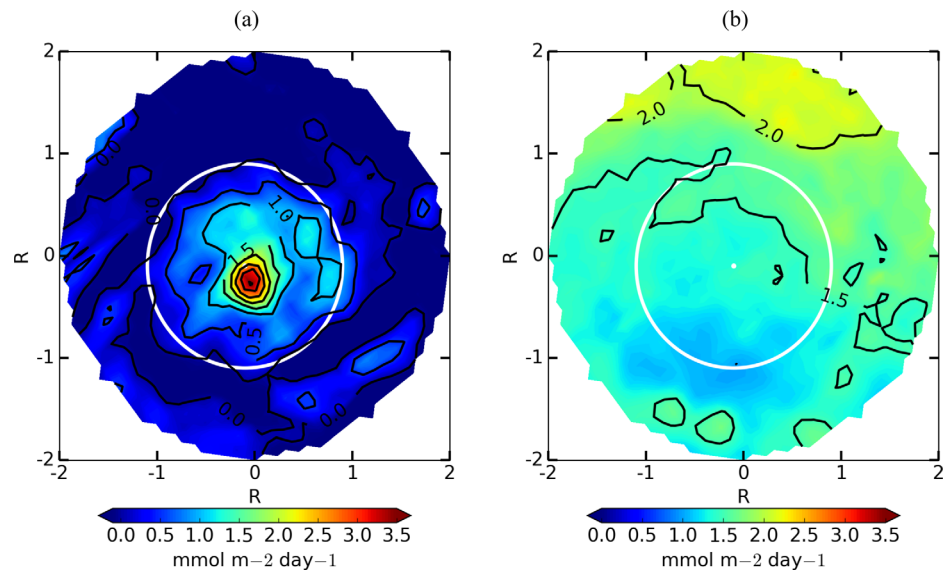


Figure 11. Composite vertical (a) advective and (b) turbulent nitrate flux associated with ACE at the base of the euphotic zone. White circles indicate the equivalent ACE radius R from the eddy center (white dot). Contour intervals are $0.5 \text{ mmol N m}^{-2} \text{ d}^{-1}$ in both plots. Note that negative value in the left plot are masked as dark blues.

advection term and the biological processes (labeled as Bio). Here, we focus on quantifying two terms: WADV and TMIX.

We start with the analyzing the physical quantities, the vertical velocity (w), and vertical mixing coefficient (κ_z) associated with ACEs, focusing on the latitudinal transect across the eddy center in the upper 200 m and the horizontal view at the euphotic depth. Inside ACEs, the vertical velocity w shows consistent upwelling with values up to 60 cm d^{-1} in the eddy center (Figure 10a). At the euphotic depth, the negative w values indicate relatively weak downwelling occurs outside ACEs (Figure 10b). The distributions of vertical mixing coefficient κ_z (Figures 10c and 10d) indicate that vertical mixing is enhanced within ACEs, which is consistent with Gaube et al. (2013) and Dufois et al. (2014, 2016).

We then proceed to examine the spatial distributions of WADV and TMIX. WADV is overall positive inside of ACE (radius smaller than R) and reaches maximum value ($3.0 \text{ mmol N m}^{-2} \text{ d}^{-1}$) at the center (Figure 11a) WADV inside of ACE is significantly higher than the surrounding waters, indicating the vertical nitrate supply into the euphotic zone is enhanced within ACEs. In contrast, the distribution of TMIX does not show that the vertical turbulent flux of nitrate is enhanced compared to the surrounding waters (Figure 11b), although the vertical mixing coefficient is enhanced within ACEs (Figures 10c and 10d). This is due to the vertical nitrate gradient weakening near the center of the ACEs (Figures 10e and 10f). The above analysis indicates that the enhanced vertical advection is the primary cause of the positive nitrate anomaly within the ACEs. The nearly vertical uniform distribution of the positive nitrate anomaly (Figure 7f) suggests that enhanced mixing in ACEs homogenize the positive nitrate anomaly between the euphotic zone and the surface layer.

To further explore the role of eddy-wind interaction-induced Ekman pumping in determining the vertical velocities inside ACEs, we create the wind stress (τ) composite over ACE based on the daily model outputs, and then derive the eddy-wind interaction-induced Ekman pumping w_E as follows:

$$w_E = -\frac{1}{\rho_0} \nabla \times \left(\frac{\tau}{f} \right),$$

where ρ_0 is the mean density ($1,025 \text{ kg m}^{-3}$) and f is the Coriolis parameter.

In our simulation, the wind stress formulation considers the surface ocean current contribution, i.e., the wind speed is relative to the ocean current (section 2.1). The composite τ over ACEs (Figure 12a) is predominantly eastward, with lower magnitude of $4.2 \times 10^{-2} \text{ N m}^{-2}$ on the north side and higher magnitude of $6.3 \times 10^{-2} \text{ N m}^{-2}$ on the south side of the eddy. The diagnosed w_E has positive values, which increase from

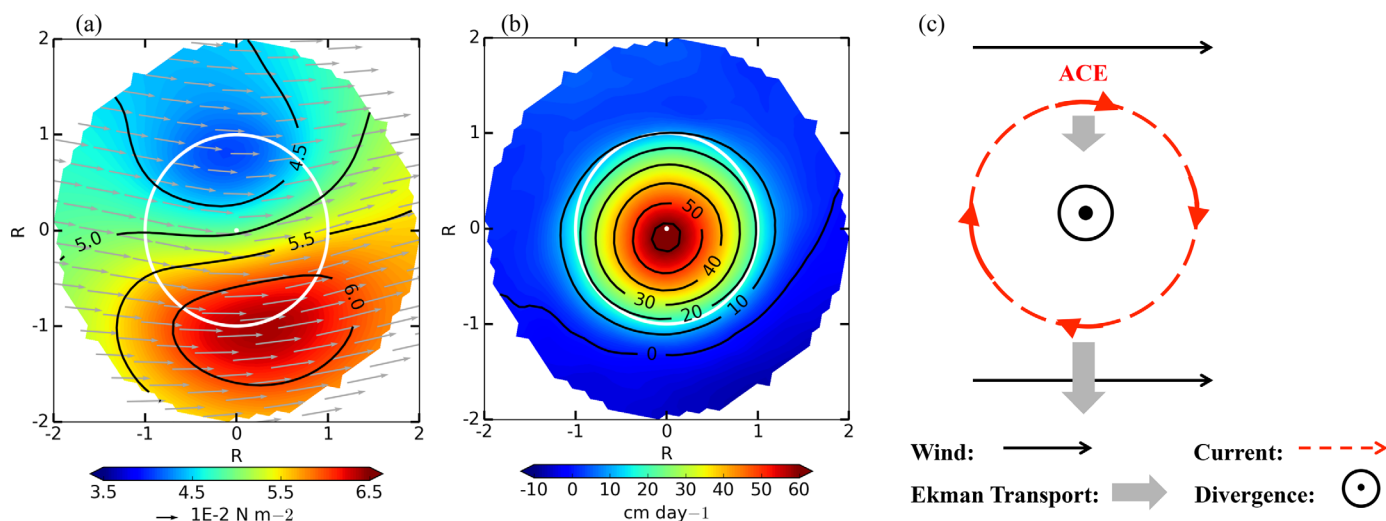


Figure 12. (a) The composite wind stress over ACEs. The magnitudes are shown as colors and directions are shown as vectors. (b) The Ekman pumping w_E derived from the curl of wind stress. (c) Schematic illustrating the eddy-wind-interaction-induced Ekman pumping (based on Figure 7 of Martin and Richards (2001)).

10 cm d^{-1} at the ACE periphery to 60 cm d^{-1} at the ACE center (Figure 12b). The magnitude and the spatial distributions of the diagnosed w_E are overall consistent with the composite of model vertical velocity at the euphotic depth (Figure 10b). This suggests that the eddy-wind interaction-induced Ekman pumping is the cause of the enhanced vertical velocity (conceptually illustrated in Figure 12c) and thus responsible for the enhanced vertical nitrate supply into euphotic zone within ACEs.

The above discussion mainly focused on the impact of eddy-wind interaction mechanism on the vertical velocity distribution in near-surface layers of ACEs. Same diagnostic calculations based on the wind stress over CE indicate that the eddy-wind interaction mechanism would lead to downwelling near the center of CEs (not shown). However, we find that the eddy-wind interaction-induced downwelling does not explain the overall positive vertical velocity and the positive nitrate anomalies in CEs obtained directly from the model results. This suggests that the eddy-pumping mechanism may overcome the eddy-wind interaction-induced downward vertical motions in CEs.

5. Summary

In this study, we conducted a 25-year eddy-resolving simulation to investigate the physical and biogeochemical properties associated with mesoscale eddies over the GS region using a recently developed coupled physical-biological model with 7 km horizontal resolution. The model was used extensively to study both the eddy characteristics generated in the study area and the three-dimensional distribution of nitrate in the eddy interior and the surrounding waters.

A Reynolds decomposition of the advection terms in the nitrate budget equation indicated that the mesoscale processes play an important role in the nitrate supply into the euphotic zone. The decomposition, however, cannot isolate eddy effects from those arising from other mesoscale phenomena (such as GS meanders and mesoscale filaments). To investigate the long-term contribution of the coherent mesoscale eddies, we extracted the hydrographic and biogeochemical fields from 612 cyclonic eddies (CEs) and 740 anticyclonic eddies (ACEs) identified during the 25-year simulation period by applying an automatic eddy detection and tracking algorithm.

Composite eddy structures indicated a significant transport of nitrate toward the surface associated with the doming of isopycnals in CEs and, in contrast, a significant concave shape of nitrate due to downwelling in ACEs below 100 m depth, which are consistent with previous studies. While above the euphotic zone depth ($\sim 62 \text{ m}$ on average), positive nitrate anomalies occur in both types of eddies, and the positive anomalies are even more pronounced in ACEs than in CEs. The long-term averaged vertical advective nitrate flux

into the euphotic zone is enhanced in both CEs and ACEs, and the vertical flux within ACEs is four times higher than that within CEs.

We have further investigated the physical mechanism responsible for the enhanced nitrate anomalies within ACEs through the model nitrate budget analysis and Ekman pumping diagnostic calculation based on model wind stress composites. The comparison of the horizontal distribution of the vertical advective flux and the vertical turbulent flux at the base of the euphotic zone indicates the positive nitrate anomaly mostly originates from the enhanced vertical advective flux. We also demonstrate that eddy-wind interaction-induced Ekman pumping is very likely the mechanism of the enhanced vertical motions within ACEs: the northward decrease of wind stress over the ACEs causes divergence and induces enhanced vertical motions near the center of ACEs.

To the best of our knowledge, this is the first study to reveal that in the GS region, ACE have positive net vertical nitrate fluxes into the euphotic zone based on a large sample of eddies detected from a long-term high-resolution simulation. The ACEs are mostly constrained between the GS and the continental shelf, which is the area characterized by high productivity. If the vertical nitrate fluxes are trapped in the eddy interior along their way propagating toward the shelf, they may fuel a significant fraction of annual new production on the shelf, as well as play an important role in primary production and other biological cycles. The response of plankton communities and primary productivities to sustaining replenishment of nutrients in the eddy interiors will be the focus of further investigation.

Acknowledgments

This study is supported by grants from NOAA-NA-15OAR4310133. Computational resources, the ROMS-COBALT model inputs and outputs used in this study are provided by Earth System Modeling lab at Rutgers University (<http://oceanis.esm.rutgers.edu:8080>); results are available on request, please contact Dr. Enrique Curchitser, curchits@envsci.rutgers.edu). We thank Dr. Bror Jonsson in Princeton University for sharing the SeaWiFS data set based on their developed retrieval algorithms to the NWA domain (for data request please contact: bjonsson@princeton.edu). We also thank Dr. Kun Gao for providing valuable help on updating eddy detection programming. The author appreciates comments and suggestions from the two anonymous reviewers and the editor, which significantly helped to improve this manuscript.

References

- Carton, J. A., & Giese, B. S. (2008). A reanalysis of ocean climate using Simple Ocean Data Assimilation (SODA). *Monthly Weather Review*, *136*, 2999–3017.
- Castelao, R. M. (2014). Mesoscale eddies in the South Atlantic Bight and the Gulf Stream Recirculation region: Vertical structure. *Journal of Geophysical Research: Oceans*, *119*, 2048–2065. <https://doi.org/10.1002/2014JC009796>
- Chelton, D., Gaube, P., Schlax, M., Early, J., & Samelson, R. (2011a). The influence of nonlinear mesoscale eddies on near-surface oceanic chlorophyll. *Science*, *334*, 328–332.
- Chelton, D., Schlax, M., & Samelson, R. (2011b). Global observations of nonlinear mesoscale eddies. *Progress in Oceanography*, *91*, 167–216.
- Chelton, D. B., Schlax, M. G., Samelson, R. M., & de Szoeke, R. A. (2007). Global observations of large oceanic eddies. *Geophysical Research Letters*, *34*, L15606. <https://doi.org/10.1029/2007GL030812>
- Chenillat, F., Franks, P., & Combes, V. (2016). Biogeochemical properties of eddies in the California Current System. *Geophysical Research Letters*, *43*, 5812–5820. <https://doi.org/10.1002/2016GL068945>
- Dewar, W. K., & Flierl, G. R. (1987). Some effects of the wind on rings. *Journal of Physical Oceanography*, *17*(10), 1653–1667.
- Dufois, F., Hardman-Mountford, N. J., Greenwood, J., Richardson, A. J., Fen, M., Herbette, S., & Matear, R. (2014). Impact of eddies on surface chlorophyll in the South Indian Ocean. *Journal of Geophysical Research: Oceans*, *119*, 8061–8077. <https://doi.org/10.1002/2014JC010164>
- Dufois, F., Hardman-Mountford, N. J., Greenwood, J., Richardson, A. J., Feng, M., & Matear, R. (2016). Anticyclonic eddies are more productive than cyclonic eddies in subtropical gyres because of winter mixing. *Science Advances*, *2*, e1600282. <https://doi.org/10.1126/sciadv.1600282>
- Eppley, R. W., & Peterson, B. J. (1979). Particulate organic matter flux and planktonic new production in the deep ocean. *Nature*, *282*(5740), 677–680.
- Falkowski, P., Ziemann, D., Kolber, Z., & Bienfang, P. (1991). Role of eddy pumping in enhancing primary production in the ocean. *Nature*, *352*(6330), 55–58.
- Garcia, H. E., Locarnini, R. A., Boyer, T. P., Antonov, J. I., Baranova, O. K., Zweng, M. M., . . . Johnson, D. R. (2014). *World Ocean Atlas 2013, Volume 4: Dissolved inorganic nutrients (phosphate, nitrate, silicate)*. S. Levitus, Ed., A. Mishonov Technical Ed. (NOAA Atlas NESDIS 76, 25 p.). Silver Spring, MD: National Oceanic and Atmospheric Administration.
- Gaube, P., Chelton, D. B., Samelson, R. M., O'neill, L. W., & Schlax, M. G. (2015). Satellite observations of mesoscale eddy-induced Ekman Pumping. *Journal of Physical Oceanography*, *45*, 104–132.
- Gaube, P., Chelton, D. B., Strutton, P. G., & Behrenfeld, M. J. (2013). Satellite observations of chlorophyll, phytoplankton biomass, and Ekman pumping in nonlinear mesoscale eddies. *Journal of Geophysical Research: Oceans*, *118*, 6349–6370. <https://doi.org/10.1002/2013JC009027>
- Gaube, P., & McGillicuddy, D. J. (2017). The influence of Gulf Stream Eddies and Meanders on near-surface chlorophyll. *Deep Sea Research, Part I*, *122*, 1–16. <https://doi.org/10.1016/j.dsr.2017.02.006>
- Gaube, P., McGillicuddy, D. J., Chelton, D. B., Behrenfeld, M. J., & Strutton, P. G. (2014). Regional variations in the influence of mesoscale eddies on near-surface chlorophyll. *Journal of Geophysical Research: Oceans*, *119*, 8195–8220. <https://doi.org/10.1002/2014JC010111>
- Joyce, T. M., Deser, C., & Spall, M. A. (2000). The relation between decadal variability of subtropical mode water and the North Atlantic Oscillation. *Journal of Climate*, *13*, 2550–2569.
- Kang, D., & Curchitser, E. N. (2013). Gulf Stream eddy characteristics in a high-resolution ocean model. *Journal of Geophysical Research: Oceans*, *118*, 4474–4487. <https://doi.org/10.1002/jgrc.20318>
- Kang, D., & Curchitser, E. N. (2015). Energetics of eddy-mean flow interactions in the Gulf Stream region. *Journal of Physical Oceanography*, *45*, 1103–1120. <https://doi.org/10.1175/JPO-D-14-0200.1>
- Kang, D., Curchitser, E. N., & Rosati, A. (2016). Seasonal variability of the Gulf Stream kinetic energy. *Journal of Physical Oceanography*, *46*, 1189–1207. <https://doi.org/10.1175/JPO-D-15-0235.1>
- Knapp, G. P. (1988). *Hydrographic data from R. V. Endeavor cruise 129* (WHOI technical reports: OCE 84-14243). <https://doi.org/10.1575/1912/7492>

- Large, W. B. (2005). Surface fluxes for practitioners of global ocean data assimilation. In E. P. Chassignet & J. Verron (Eds.), *Ocean weather forecasting: An integrated view of oceanography* (Vol. 577, pp. 229–270). The Netherlands: Springer.
- Large, W. G., & Yeager, S. G. (2009). The global climatology of an interannually varying air-sea flux data set. *Climate Dynamics*, 33, 341–364. <https://doi.org/10.1007/s00382-008-0441-3>
- Martin, A., & Richards, K. (2001). Mechanisms for vertical nutrient transport within a North Atlantic mesoscale eddy. *Deep Sea Research, Part II*, 48(4–5), 757–773.
- Mayorga, E., Seitzinger, S. P., Harrison, J. A., Dumont, E., Beusen, A. H. W., Bouwman, A. F., . . . Van Drecht, G. (2010). Global Nutrient Export from Watersheds 2 (NEWS 2): Model development and implementation. *Environmental Modelling & Software*, 25(7), 837–853. <https://doi.org/10.1016/j.envsoft.2010.01.007>
- McGillicuddy, D. J. (2016). Mechanisms of physical-biological-biogeochemical interaction at the oceanic mesoscale. *Annual Review of Marine Science*, 8, 125–159.
- McGillicuddy, D. J., Anderson, L. A., Bates, N. R., Bibby, T., Buesseler, K. O., Carlson, C. A., . . . Steinberg, D. K. (2007). Eddy/wind interactions stimulate extraordinary mid-ocean plankton blooms. *Science*, 316(5827), 1021.
- McGillicuddy, D. J., Anderson, L. A., Doney, S. C., & Maltrud, M. E. (2003). Eddy-driven sources and sinks of nutrients in the upper ocean: Results from a 0.1° resolution model of the North Atlantic. *Global Biogeochemical Cycles*, 17(2), 1035. <https://doi.org/10.1029/2002GB001987>
- McGillicuddy, D. J. Jr., Johnson, R., Siegel, D. A., Michaels, A. F., Bates, N. R., & Knap, A. H. (1999). Mesoscale variations of biogeochemical properties in the Sargasso Sea. *Journal of Geophysical Research*, 104, 13,381–13,394. <https://doi.org/10.1029/1999JC900021>
- McGillicuddy, D. J. Jr., & Robinson, A. R. (1997). Eddy induced nutrient supply and new production in the Sargasso Sea. *Deep Sea Research, Part I*, 44, 1427–1449.
- McGillicuddy, D. J. Jr., Robinson, A. R., Siegel, D. A., Jannasch, H. W., & Johnson, R. (1998). Influence of mesoscale eddies on new production in the Sargasso Sea. *Nature*, 394, 263–265.
- Nagai, T., Gruber, N., Frenzel, H., Lachkar, Z., McWilliams, J. C., & Plattner, G.-K. (2015). Dominant role of eddies and filaments in the offshore transport of carbon and nutrients in the California Current System. *Journal of Geophysical Research: Oceans*, 120, 5318–5341. <https://doi.org/10.1002/2015JC010889>
- NASA Goddard Space Flight Center, Ocean Biology Processing Group (2014). *Sea-viewing Wide Field-of-view Sensor (SeaWiFS) ocean color data*. Greenbelt, MD: NASA Ocean Biology Distributed Active Archive Center (OB.DAAC), Goddard Space Flight Center. https://doi.org/10.5067/ORBVIEW-2/SEAWIFS_OC.2014.0
- Olson, D. B., Schmitt, R. W., Kennelly, M., & Joyce, T. M. (1985). A two-layer diagnostic model of the long-term physical evolution of warm core ring 82B. *Journal of Geophysical Research*, 90, 8813–8822. <https://doi.org/10.1029/JC090iC05p08813>
- Richardson, P. L. (1983). Gulf Stream rings. In A. R. Robinson (Ed.), *Eddies in marine science. Topics in atmospheric and oceanographic sciences*. Berlin, Heidelberg: Springer.
- Richardson, P. L. (1993). A census of eddies observed in North Atlantic SOFAR float data. *Progress in Oceanography*, 31, 1–50. [https://doi.org/10.1016/0079-6611\(93\)90022-6](https://doi.org/10.1016/0079-6611(93)90022-6)
- Shchepetkin, A. F., & McWilliams, J. C. (2005). The Regional Oceanic Modeling System (ROMS): A split-explicit, free-surface, topography-following-coordinate oceanic model. *Ocean Modelling*, 9, 347–404.
- Siegel, D. A., Peterson, P., McGillicuddy, D. J. Jr., Maritorena, S., & Nelson, N. B. (2011). Bio-optical footprints created by mesoscale eddies in the Sargasso Sea. *Geophysical Research Letters*, 38, L13608. <https://doi.org/10.1029/2011GL047660>
- Stock, C. A., Dunne, J. P., & John, J. G. (2014a). Drivers of trophic amplification of ocean productivity trends in a changing climate. *Biogeosciences*, 11, 7125–7135. <https://doi.org/10.5194/bg-11-7125-2014>
- Stock, C. A., Dunne, J. P., & John, J. G. (2014b). Global-scale carbon and energy flows through the marine planktonic food web: An analysis with a coupled physical-biological model. *Progress in Oceanography*, 120, 1–28. <https://doi.org/10.1016/j.pocean.2013.07.001>
- Stock, C. A., John, J. G., Rykaczewski, R. R., Asch, R. G., Cheung, W. W. L., Dunne, J. P., . . . Watson, R. A. (2017). Reconciling fisheries catch and ocean productivity. *Proceedings of the National Academy of Sciences*, 114, E1441–E1449. <https://doi.org/10.1073/pnas.1610238114>
- Talley, L., Pickard, G. L., Emery, W. J., & Swift, J. H. (2011). *Descriptive physical oceanography: An introduction* (6th ed.). Cambridge, MA: Academic Press.
- Taylor A. H., & Stephens J. A. (1998). The North Atlantic oscillation and the latitude of the Gulf Stream. *Tellus A: Dynamic Meteorology and Oceanography*, 50, 134–142.
- Townsend, D. W., & Ellis, W. G. (2010). Primary production and nutrient cycling on the north-west Atlantic continental shelf. In K.-K. Liu, L. Atkinson, R. Quiñones, and L. Talaue-McManus (Eds.), *Carbon and nutrient fluxes in continental margins: A global synthesis* (pp. 234–248). New York, NY: Springer.
- Woodward, E. M. S., & Rees, A. P. (2001). Nutrient distributions in an anticyclonic eddy in the northeast Atlantic Ocean, with reference to nanomolar ammonium concentrations. *Deep Sea Research, Part II*, 48, 775–793.